Nano Research 2017, 10(8): 2633–2643
DOI 10.1007/s12274-017-1466-x
Research Article
ISSN 1998-0124
CN 11-5974/O4

Intercalated 2D nanoclay for emerging drug delivery in cancer therapy

Yi Zhang[1,§], Mei Long[1,§], Peng Huang[2,§], Huaming Yang[1,3] (✉), Shi Chang[2] (✉), Yuehua Hu[1,3] (✉), Aidong Tang[4], and Linfeng Mao[2]

[1] *Department of Inorganic Materials, School of Minerals Processing and Bioengineering, Central South University, Changsha 410083, China*
[2] *Xiangya Hospital, Central South University, Changsha 410078, China*
[3] *Hunan Key Laboratory of Mineral Materials and Application, Central South University, Changsha 410083, China*
[4] *School of Chemistry and Chemical Engineering, Central South University, Changsha 410083, China*
[§] *These authors contributed equally to this work.*

Received: 9 October 2016
Revised: 25 December 2016
Accepted: 30 December 2016

KEYWORDS
cancer therapy,
nanoclay,
intercalation,
drug delivery,
biocompatibility

ABSTRACT

Natural two-dimensional (2D) kaolinite nanoclay has been incorporated into an emerging drug delivery system. The basal spacing of the kaolinite nanoclay was expanded from 0.72 to 4.16 nm through the intercalation of various organic guest species of different chain lengths, which can increase the efficiency in drug delivery and reduce the toxicity of doxorubicin (DOX). Original kaolinite (Kaolin) and the Kaolin intercalation compounds exhibited a high level of biocompatibility and very low toxicity towards cells of pancreatic cancer, gastric cancer, prostate cancer, breast cancer, colorectal cancer, esophageal cancer, and differentiated thyroid cancer. However, lung cancer and hepatocellular cancer cells need more strict compositional, structural, and morphological modulations for drug delivery carriers. DOX-Kaolin and the DOX-Kaolin intercalation compounds showed dramatically faster drug release in moderately acidic solution than in neutral condition, and exhibited enhanced therapeutic effects against ten model cancer cell cultures in a dose-dependent manner. The use of 2D nanoclay materials for a novel drug delivery system could feasibly pave a way towards high-performance nanotherapeutics, with superior antitumor efficacy and significantly reduced side effects.

1 Introduction

From bench to clinic, emerging drug delivery systems (DDSs) against cancers require technical support and several long-term trials [1–3]. The remarkable progress of nanotechnology and its application in biomedicine have greatly expanded the range and type of biomaterials for medical use from traditional natural

Address correspondence to Huaming Yang, hmyang@csu.edu.cn; Shi Chang, changshi@csu.edu.cn; Yuehua Hu, hyh@csu.edu.cn

materials to emerging organic or inorganic synthetic products. Organic materials (liposomes [4, 5], metal-organic frameworks [6, 7], chitosans [8, 9], etc.) are now relatively mature in their clinical translation after decades of development, and have been commercially driven to the clinical stage for tumor chemotherapy. However, the intrinsic instability and low drug-loading capacity/efficiency of organic DDSs leave many of them in the preclinical stage and inhibit their further clinical translation. Inorganic materials have shown unique characteristics of high thermal/chemical stability and resistance to corrosion under physiological conditions. Various inorganic materials, such as magnetic nanoparticles [10–13], carbon-based nanomaterials [14–16], mesoporous silica nanoparticles [17–21], layered double hydroxides [22–24], etc., showed excellent biocompatibility but had relatively low degradation rates.

Clay minerals, most notably halloysite [25–32], montmorillonite [33, 34], diatomite [35–37], kaolinite [38–40], talc [41], and palygorskite [42], have attracted increasing attention for application in nanocomposite synthesis, especially for the biomedical fields. Inspired by traditional Chinese medicine, a detailed description of each clay mineral's name, source, shape, color, and method of collection has been recorded by Shizhen Li in the Compendium of Materia Medica. Kaolinite, $Al_2Si_2O_5(OH)_4$ (Kaolin), one of the most representative and well-established clay minerals, is a two-dimensional (2D) aluminosilicate with a structure consisting of $AlO_2(OH)_4$ octahedral sheets and SiO_4 tetrahedral sheets in a 1:1 ratio [43]. A prerequisite for the fundamental understanding of kaolinite-based DDSs is knowledge of the biostability, biocompatibility, and degradability of the kaolinite clay, which are still ambiguous.

In this paper, Kaolin and Kaolin intercalation compound-based DDSs were prepared through intercalation of various organic guest species of different chain lengths (short-chain dimethyl sulfoxide (DMSO) and methanol (MeOH), medium-chain hexylamine (C_6N) and 3-aminopropyltriethoxysilane (APTES), and long-chain dodecylamine ($C_{12}N$)), because intercalation technology is the general modification method used for kaolinite (Fig. 1). The expanded basal spacing of kaolinite provides a sufficiently spacious site for hosting molecules of the anticancer drug doxorubicin (DOX)

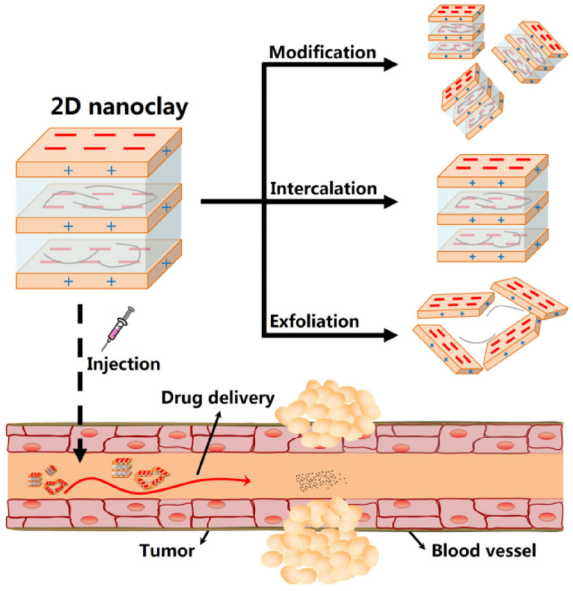

Figure 1 Schematic diagram of Kaolin and the Kaolin intercalation compounds used for tumor therapy.

and controlling its release rate, which could increase the delivery efficiency and reduce the drug's toxicity. The interfacial relationships between kaolinite and organic compounds, the drug-loading efficiency, and the biocompatibility and toxicity of Kaolin and Kaolin intercalation compounds towards cancer cells were investigated. Intracellular uptake by cells of different cancers (lung cancer, breast cancer, colorectal cancer, gastric cancer, prostate cancer, hepatocellular cancer, cervical cancer, esophageal cancer, pancreatic cancer, and thyroid cancer) and cell viability tests demonstrated the fabricated 2D nanoclays to have a high level of biocompatibility, very low cytotoxicity, and potential as biofriendly DDSs for biomaterials.

2 Experimental

2.1 Synthesis of Kaolin intercalation compounds

Intercalation of kaolinite with other compounds was done according to previously published procedures. DMSO-intercalated kaolinite ($Kaolin_{DMSO}$) was synthesized by dispersing the mineral into neat liquid DMSO at 60 °C for 12 h. MeOH-intercalated kaolinite ($Kaolin_{MeOH}$) was prepared by reacting 5.0 g of $Kaolin_{DMSO}$ with 100 mL of MeOH at room temperature. The MeOH was refreshed every day for 7 days. C_6N-intercalated kaolinite ($Kaolin_{C6N}$) and $C_{12}N$-intercalated kaolinite

($Kaolin_{C12N}$) were prepared by stirring mixtures of the respective alkylamines with $Kaolin_{MeOH}$ at 60 ℃ for 3 days. APTES-intercalated kaolinite ($Kaolin_{APTES}$) was prepared by stirring a mixture of APTES and $Kaolin_{MeOH}$ at 50 ℃ for 3 days. The $Kaolin_{MeOH}$ was used without any drying processes.

2.2 DOX loading and *in vitro* release of DOX from Kaolin intercalation compounds under different pH conditions

The Kaolin intercalation compounds (5 mg) were respectively dispersed in 6 mL of 0.5 mg·mL^{-1} DOX (in phosphate-buffered saline (PBS) solution) for 24 h in the dark. Then, the mixture was separated, stored, and labeled. The loading rate was evaluated through measurement of the residual DOX solution by UV–Vis spectroscopy at a wavelength of 485 nm. For *in vitro* DOX release assessment, 2 mg of each DOX-Kaolin intercalation compound was first packaged in a dialysis bag and then immersed in 15 mL of PBS solutions with different pH values (pH = 7.4, 5.5, and 4.5). The release rate was monitored by UV–Vis spectroscopy over time.

2.3 MTS assay

In vitro cytotoxicity and cell proliferation were evaluated by MTS (3-(4,5-dimethylthiazol-2-yl)-2,5-diphenyltetrazolium bromide) reduction assays. The cells were first incubated with RPMI-1640 medium at 37 ℃ in 5% CO_2 for 24 h, following which fresh medium containing the nanocomposites (0, 50, 100, or 200 μg·mL^{-1}) was added and the cells were further incubated for 24 h. Then, 20 μL of MTS working liquid was added per well and the plate was incubated for 3 h, after which the colorimetric readout was determined at 490 nm. The cytotoxicity was assessed by comparing the percentage of viable cells in the treated cultures with that in the untreated control culture. Finally, the cell nuclei were stained with 4′,6-diamidino-2-phenylindole (DAPI) and observed under a fluorescence microscope (Leica, Germany).

2.4 Confocal laser scanning microscopy observations (CLSM)

The cells were first incubated in a special CLSM culture dish at 37 ℃ in 5% CO_2 until the cell density reached 60%–70%, following which fresh medium containing the nanocomposite (2 mL, 50 μg·mL^{-1}) was added and the cells were further incubated for 4 h. Then, the cells were washed and detached, and the nuclei were stained with DAPI for viewing by CLSM (SP8; Leica).

2.5 Characterization of the fabricated 2D nanoclays

Transmission electron microscopy (TEM) images were obtained using a JEOL JEM-200CX instrument. Nitrogen gas adsorption–desorption isotherms were measured at –196 ℃ using a Micromeritics ASAP 2020 sorptometer. The specific surface area was calculated using Brunauer–Emmett–Teller (BET) theory, and the total pore volume was estimated from the amount adsorbed at the relative pressure of approximately 0.99. The pore size distribution curves were calculated from the analysis of the adsorption branch of the isotherm, using the Barrett–Joyner–Halenda (BJH) algorithm. X-ray diffraction (XRD) patterns were obtained with the use of a Rigaku D/max 2550 system, with Cu Kα radiation (λ = 0.15406 nm) over the 2θ scanning ranges of 1°–10° for small-angle XRD at a voltage of 40 kV and 300 mA, and 10°–70° for wide-angle XRD at a voltage of 40 kV and 200 mA, both with a step width of 0.02°. Fourier transform infrared spectra (FTIR) of the samples were obtained by using the Nexus-670 spectrometer with a nominal resolution of 2 cm^{-1}.

3 Results and discussion

3.1 Morphology and structure of Kaolin and the Kaolin intercalation compounds

Kaolin had a typical pseudo-hexagonal flaked morphology and was 400–500 nm in diameter (Figs. 2(a) and 2(b)). The water contact angle of original kaolinite was about 23° (Fig. 2(c)), indicating that Kaolin is hydrophilic and easily dispersed in water. After intercalation, the thickness of the layers was significantly reduced, but the flaked morphology was preserved. In the cases of $Kaolin_{DMSO}$ and $Kaolin_{MeOH}$, the flaked morphology was preserved, but the thickness was reduced. On the other hand, the edges of the kaolinite layer were partially curled in $Kaolin_{C6N}$ and $Kaolin_{C12N}$, concurrent with varying degrees of swelling. The

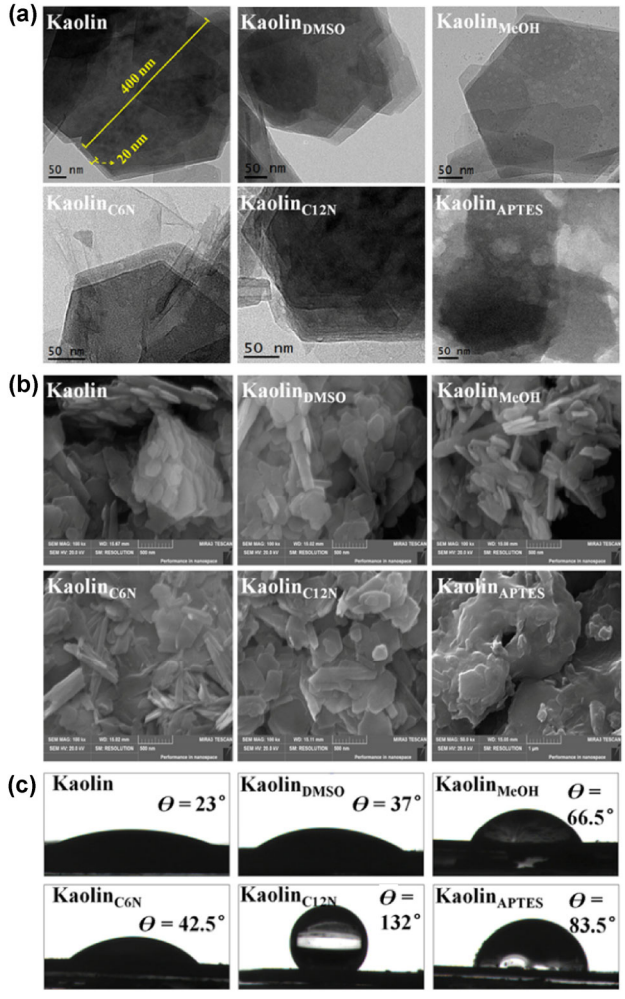

Figure 2 (a) TEM images, (b) SEM images, and (c) wetting behavior of Kaolin and the Kaolin intercalation compounds.

contrast of the TEM images of Kaolin$_{APTES}$ was relatively low, which was attributed to the residual organic compound affecting the microscopic resolution.

With regard to the hydrophobicity and hydrophilicity, the intercalation of kaolinite with DMSO, MeOH, C_6N, and APTES resulted in water contact angles lower than 90° (37°, 66.5°, 42.5°, and 83.5°, respectively) (Fig. 2(c)), indicating that the Kaolin intercalation compounds still had hydrophilicity, albeit much lower. However, Kaolin$_{C12N}$ revealed a hydrophobic surface with the high apparent contact angle of 132°. The hydrophilicity of Kaolin and the Kaolin intercalation compounds had a great influence not only on the adhesion and proliferation of cells but also on the loading and release of the anticancer drug.

The XRD patterns indicated that the original kaolinite had a typical diffraction pattern, with a characteristic d_{001} value of 0.72 nm (Fig. 3(a) and Fig. S1(a) in the Electronic Supplementary Material (ESM)). The grafting of DMSO into the interlayer space of kaolinite resulted in a d_{001} value of 1.12 nm for Kaolin$_{DMSO}$. Kaolin$_{MeOH}$ had a decreased basal spacing of 0.86 nm due to its use of the DMSO-treated kaolinite intercalation complex as an intermediate. The remaining reflection at 0.72 nm was due to residual un-intercalated kaolinite. A larger basal spacing was obtained by interacting APTES, C_6N, and $C_{12}N$ with wet Kaolin$_{MeOH}$, with the corresponding d_{001} values being increased to 2.18, 2.63, and 4.16 nm, respectively. The additional peaks in Kaolin$_{APTES}$ and Kaolin$_{C6N}$ were assigned to the un-intercalated kaolinite or residual organic compounds. The sharp reflection peak next to that of 4.16 nm and some other non-obvious peaks in Kaolin$_{C12N}$ were attributed to a crystalline-free dodecylamine. The increased basal spacing within the Kaolin intercalation compounds could lead to more negatively charged Si–OH residues of exposed kaolinite, which is beneficial to the controlled release of the positively charged DOX molecules, thereby reducing the toxicity and promoting the efficiency of DOX in this DDS.

The FTIR spectra of the 2D clays were used to further prove the success of intercalation (Fig. 3(b) and Fig. S1(b) in the ESM). The original kaolinite exhibited three –OH stretching bands at 3,694, 3,654, and 3,620 cm^{-1}. The bands at 3,694 and 3,654 cm^{-1} were assigned to the O–H stretching of inner-surface hydroxyl groups, and the band at 3,620 cm^{-1} was attributed to the O–H stretching of inner hydroxyl groups. After intercalation, the intensities of the three inner-surface hydroxyl groups were weakened, and new characteristic IR peaks of the guest species appeared. For Kaolin$_{DMSO}$, the bands at 3,670 and 3,654 cm^{-1} were due to the inner surface –OH and out-of-phase stretching vibration, respectively. The C–H stretching vibration band at 2,938 cm^{-1} was a result of the DMSO molecules. For Kaolin$_{MeOH}$, the C–H stretching vibration band of the surface methoxy groups was at 2,848 cm^{-1}. For Kaolin$_{C6N}$, the band at 2,957 cm^{-1} was attributed to the C–H stretching vibration of methyl groups, and the bands at 2,927 and 2,850 cm^{-1} were due to the C–H stretching vibration of the surface methoxy groups. The remaining C–H stretching vibration band of the surface methoxy

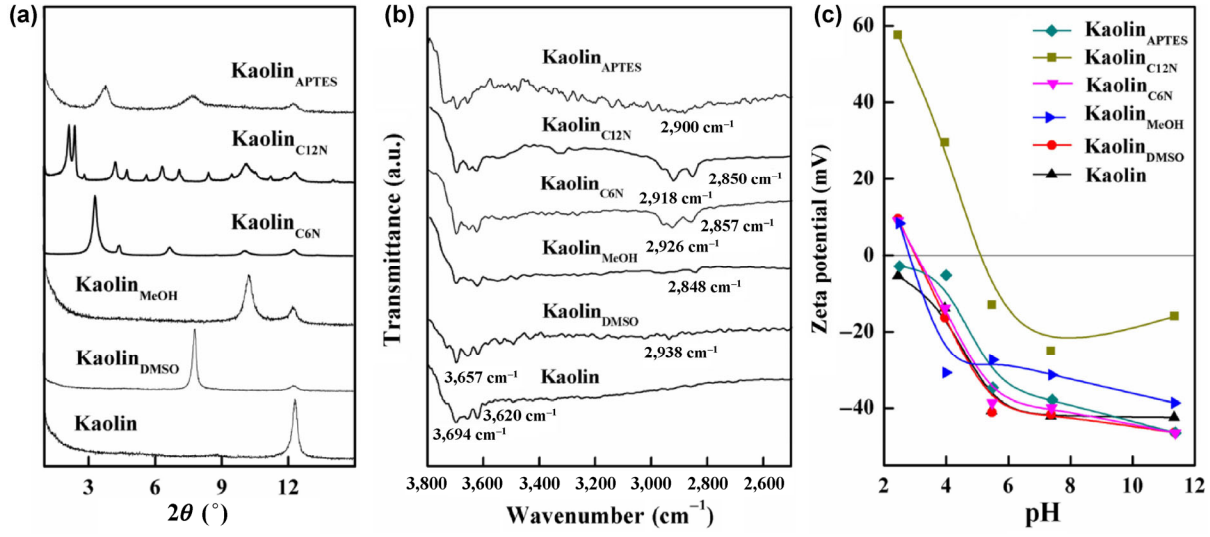

Figure 3 (a) XRD patterns, (b) FTIR spectra, and (c) zeta potential at various pH values of Kaolin and the Kaolin intercalation compounds.

groups was due to the residual un-intercalated $Kaolin_{MeOH}$. For $Kaolin_{C12N}$, the band at 3,328 cm^{-1} was assigned to the O–H or N–H stretching vibration. The bands at 2,918 and 2,850 cm^{-1} were assigned to the C–H stretching vibration of the methyl group and the surface methoxy group, respectively. For $Kaolin_{APTES}$, the band at 2,925 cm^{-1} was assigned to the C–H stretching vibration.

The zeta potentials for Kaolin and the Kaolin intercalation compounds were measured as a function of pH (Fig. 3(c)). Original kaolinite had negative surface charges (–42.7 to –5.7 mV), indicating good dispersion stability, and had larger negative zeta potentials at high pH. After intercalation, the zeta potentials were not affected, except for $Kaolin_{C12N}$. The observed zeta potentials of $Kaolin_{DMSO}$, $Kaolin_{MeOH}$, $Kaolin_{C6N}$, $Kaolin_{C12N}$, and $Kaolin_{APTES}$ ranged from 9.6 to –46.3, 8.3 to –38.8, 8.9 to –46.5, 57.4 to –16.2, and –2.9 to –46.4 mV, respectively. The corresponding isoelectric points of $Kaolin_{DMSO}$, $Kaolin_{MeOH}$, $Kaolin_{C6N}$, and $Kaolin_{C12N}$ were 3.1, 2.8, 3.1, and 5.2, respectively. The negative charges of Kaolin and the Kaolin intercalation compounds provided sites for complexation with the positively charged DOX via electrostatic interaction. Thereby, the drug-loading procedure can be efficiently carried out in an aqueous medium without the use of toxic reagents or organic solvents, representing a green chemistry approach.

Table 1 and Fig. S2(a) in the ESM show the N_2 adsorption isotherms of kaolinite and its intercalation compounds. Pure kaolinite exhibited a H3-type hysteresis loop at a relative pressure (p/p_0) of >0.6. For $Kaolin_{DMSO}$, $Kaolin_{MeOH}$, and $Kaolin_{C6N}$, the appearance of the adsorption/desorption hysteresis showed no difference to that of Kaolin. However, $Kaolin_{APTES}$ and $Kaolin_{C12N}$ exhibited a type IV isotherm at the p/p_0 of ~0.05 and a large hysteresis loop. In addition, the values of the BET surface area (S_{BET}) of Kaolin, $Kaolin_{DMSO}$, $Kaolin_{MeOH}$, $Kaolin_{C6N}$, $Kaolin_{C12N}$, and $Kaolin_{APTES}$ were 25.16, 22.15, 16.23, 47.56, 14.42, and 19.42 $m^2 \cdot g^{-1}$, respectively. The total pore volume of Kaolin, $Kaolin_{DMSO}$, $Kaolin_{MeOH}$, $Kaolin_{C6N}$, $Kaolin_{C12N}$,

Table 1 Porous textures of Kaolin and the Kaolin intercalation compounds

Sample	Kaolin	$Kaolin_{DMSO}$	$Kaolin_{MeOH}$	$Kaolin_{C6N}$	$Kaolin_{C12N}$	$Kaolin_{APTES}$
S_{BET} ($m^2 \cdot g^{-1}$)	25.16	22.15	16.23	47.56	19.42	14.42
V_T ($mL \cdot g^{-1}$)	0.09	0.08	0.08	0.23	0.01	0.02
D_A (nm)	14.90	14.31	20.21	19.51	1.49	4.77

and $Kaolin_{APTES}$ were 0.09, 0.08, 0.08, 0.23, 0.02, and 0.01 $mL \cdot g^{-1}$, respectively. The lower S_{BET} and pore volume was possibly related to the kaolinite microstructure in the Kaolin intercalation compounds and unwashed residual organic compounds (Fig. S2(b) in the ESM). Intercalation of various organic guest species of different chain lengths decreased the surface area of Kaolin, which could slow the drug release rate.

3.2 Release behavior of Kaolin and the Kaolin intercalation compounds *in vitro*

To investigate the potential of the 2D Kaolin clays as promising drug delivery carriers, DOX was introduced as a model anticancer agent and loaded onto Kaolin and the Kaolin intercalation compounds. The negatively charged surface of all the fabricated clays under neutral condition could facilitate the loading of positively charged DOX molecules. The DOX-loading efficiency of Kaolin, $Kaolin_{DMSO}$, $Kaolin_{MeOH}$, $Kaolin_{C6N}$, $Kaolin_{C12N}$, and $Kaolin_{APTES}$ was 90.69%, 90.39%, 90.86%, 90.32%, 87.65% and 92.61%, respectively. $Kaolin_{C12N}$ showed the lowest DOX-loading efficiency, attributed to its hydrophobicity and larger particle size. The *in vitro* drug release capabilities of the DOX-loaded Kaolin and Kaolin intercalation compounds are shown in Table 2 and Fig. S3 in the ESM. The assays revealed that drug release from the Kaolin and Kaolin intercalation compounds in moderately acidic solution was dramatically faster than that in neutral condition. For the buffer solution at pH 4.5, the DOX-Kaolin intercalation compounds exhibited a controlled release of DOX, where the highest cumulative release was 43.85% from Kaolin, 20.44% from $Kaolin_{DMSO}$, 35.87% from $Kaolin_{MeOH}$, 22.26% from $Kaolin_{C6N}$, 29.20% from $Kaolin_{C12N}$, and 28.39% from $Kaolin_{APTES}$. The cumulative release from Kaolin, $Kaolin_{DMSO}$, $Kaolin_{MeOH}$, $Kaolin_{C6N}$, $Kaolin_{C12N}$, and $Kaolin_{APTES}$ at pH 5.5 was 21.74%, 11.09%, 19.95%, 18.61%, 11.20%, and 10.89%, respectively, whereas that at pH 7.4 was 4.18%, 5.50%, 5.73%, 5.92%, 2.96%, and 2.37%, respectively. DOX release from the modified kaolinite exhibited typical sustained pH-responsive release profiles, which could be attributed to the dissociation of electrostatic interaction between the positively charged DOX molecules and the negatively charged Si–OH moiety of Kaolin and the Kaolin intercalation compounds that is protonated at low pH values. This pH-responsive release behavior could be used to increase targeting of the drug delivery to cancer tissues and to diminish the drug's side effects, since the pH of blood is neutral (pH = 7.4) whereas that of the tumor extracellular condition is acidic (pH = 6.5) and the endosome-lysosome condition is even more acidic (pH = 5.0–5.5).

To understand the mechanism of DOX release from the drug-loaded Kaolin and Kaolin intercalation compounds, the semiempirical equation of Korsmeyer–Peppas ($M_t/M_\infty = kt^n + b$) was used to fit the accumulative release data. In this model, Fickian diffusion through a slab is indicated by a diffusional exponent (n) of 0.50, whereas an anomalous transport (non-Fickian) mechanism is indicated by an n value of 0.50–1.0. Parameters obtained by this equation for each sample release profile are summarized in Table 2. The coefficients fitted by the modified Korsmeyer–

Table 2 Parameters of the Korsmeyer–Peppas model of cumulative DOX release from DOX-Kaolin and the DOX-Kaolin intercalation compounds

Sample	Loading amount (%)	Cumulative release (%, pH = 4.5, 5.5, 7.4)	pH = 4.5 (n, k, b)[a]	pH = 5.5 (n, k, b)[a]	pH = 7.4 (n, k, b)[a]
Kaolin	54.41	43.84, 21.74, 4.18	0.46, 9.67, –1.58	0.54, 3.74, –1.19	0.39, 1.15, –0.23
$Kaolin_{DMSO}$	54.24	20.44, 11.09, 5.50	0.44, 4.82, –0.42	0.47, 2.56, –0.88	1.65, 0.02, –0.17
$Kaolin_{MeOH}$	54.52	35.87, 19.95, 5.73	0.42, 9.05, –1.30	0.55, 3.03, –0.86	0.58, 0.59, –0.26
$Kaolin_{C6N}$	54.19	22.26, 18.61, 5.92	0.38, 6.39, –0.86	0.39, 5.25, –0.83	0.42, 1.50, –0.42
$Kaolin_{C12N}$	52.59	29.20, 11.2, 2.96	0.41, 8.11, –1.37	0.33, 4.02, –0.52	0.43, 0.64, –0.67
$Kaolin_{APTES}$	55.57	28.39, 10.89, 2.37	0.4, 7.27, –0.79	0.46, 2.22, –0.60	0.49, 0.47, –0.12

[a] n is the release exponent characteristic of the release mechanism, k is a constant that incorporates the structural and geometric characteristics of the drug dosage form, and b represents the burst effect in the release.

Peppas model were relative ideal. The k values for the DOX-Kaolin intercalation compounds were much smaller than the value for DOX-Kaolin (9.67, 3.74, and 1.15 at pH of 4.5, 5.5, and 7.4, respectively), indicating a much slower release of DOX from the intercalated-Kaolin nanoclays than that from Kaolin. The release exponent (n) of each sample in the pH 4.5 solution was around 0.5, indicating that the release mechanism was Fickian diffusion. On the other hand, some n values at pH 5.5 and 7.4 were found to be higher than 0.5, showing that the DOX transport process was anomalous, corresponding to a pseudo-Fickian or Case III mechanism.

3.3 Biocompatibility of Kaolin and Kaolin intercalation compounds

Ten model cancer cell lines, including lung cancer, pancreatic cancer, gastric cancer, hepatocellular cancer, prostate cancer, breast cancer, cervical cancer, colorectal cancer, esophageal cancer, and differentiated thyroid cancer cells, were used to evaluate the biocompatibility of the fabricated clays due to their different physicochemical characteristics. The cytocompatibility of Kaolin and the Kaolin intercalation compounds with the ten model cell cultures, at the concentrations of 200 μg·mL^{-1}, is shown in Fig. 4 and Fig. S4 in the ESM. For original Kaolin, the percentage viability of the cell lines was mostly above 85%, where that of esophageal cancer reached up to 99.8%, whereas that of lung cancer was only 61.3%. In the presence of Kaolin$_{DMSO}$, the cell viabilities were mostly above 90%, whereas that of lung cancer was 87.9%. For Kaolin$_{MeOH}$, the cell viabilities were above 95%, indicating that this nanoclay had the highest level of biocompatibility and lowest toxicity towards the ten model cancer cells. For Kaolin$_{C6N}$, the cell viabilities were mostly above 90%, except for those of hepatocellular cancer and cervical cancer, which were 70.1% and 83.7%, respectively. For Kaolin$_{APTES}$, the cell viabilities were mostly above 90%, except for that of hepatocellular cancer, which was 86.2%. For Kaolin$_{C12N}$, the cell viabilities were around 90%, except for that of lung cancer, which was only 61.3%. The pancreatic, gastric, prostate, breast, colorectal, esophageal, cervical, and differentiated thyroid cancer cells exhibited almost no biological rejection of Kaolin and the Kaolin intercalation compounds. However, the lung and hepatocellular cancer cells needed more strict compositional, structural, and morphological modulations for drug delivery carriers. The results indicated that Kaolin and the Kaolin intercalation compounds have a high level of biocompatibility and very low toxicity towards most cancer cells, rendering them as promising candidates for emerging DDSs and tissue engineering applications.

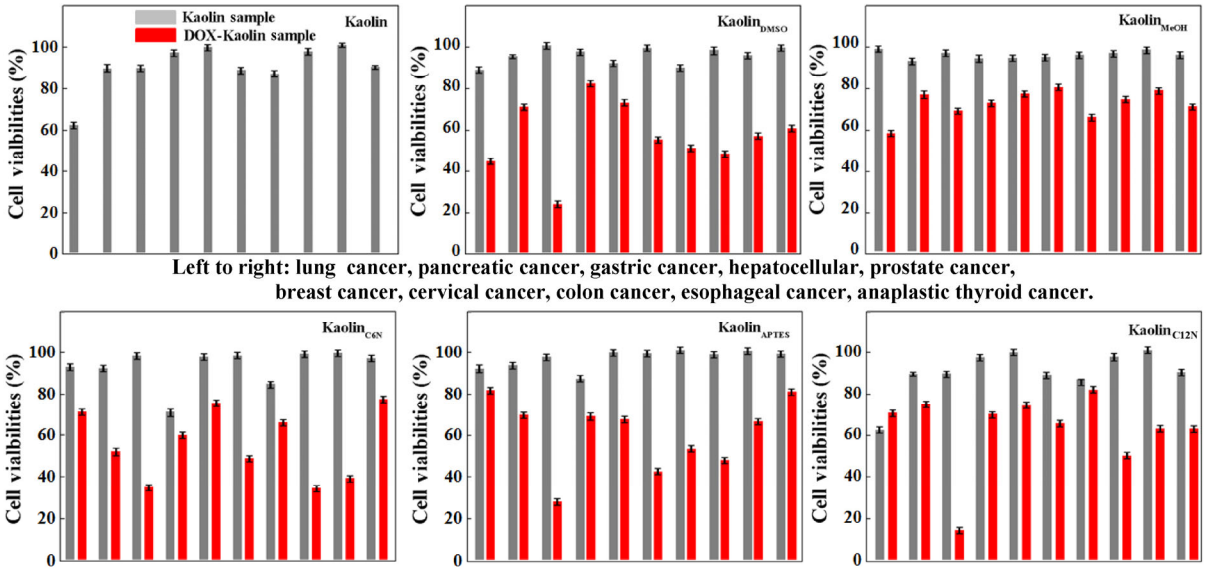

Figure 4 Viability counts of ten model cancer cell cultures after incubation with Kaolin, Kaolin intercalation compounds, and DOX-Kaolin intercalation compounds at the concentrations of 200 μg·mL^{-1}.

In addition, the quantitative growth inhibition of free DOX, DOX-Kaolin, and the DOX-Kaolin intercalation compounds against the ten model cancer cells are shown in Fig. 4 and Fig. S4 in the ESM. For DOX-Kaolin$_{DMSO}$, the cell viabilities were between 40% and 70%, showing obvious inhibition of gastric cancer with 23% cell viability, but less effectiveness against hepatocellular cancer with 80% cell viability. For DOX-Kaolin$_{MeOH}$, the cell viabilities were between 60% and 80%, where those of prostate cancer, breast cancer, and esophageal cancer were nearly 80%, indicating the weak cancer inhibition effect of this clay. For DOX-Kaolin$_{C6N}$, the cell viabilities were between 35% and 75%, where those of hepatocellular cancer, colon cancer, and esophageal cancer were around 35%. However, this nanoclay showed weak inhibition of lung cancer, prostate cancer, and differentiated thyroid cancer, with cell viabilities of 70%, 74%, and 76%, respectively. For DOX-Kaolin$_{C12N}$, the cell viabilities were between 15% and 85%, showing obvious inhibition of gastric cancer with 13% cell viability, and less effectiveness against cervical cancer with 80% cell viability. For DOX-Kaolin$_{APTES}$, the cell viabilities were between 40% and 60%, where the nanoclay showed obvious inhibition of gastric cancer with 27% cell viability, and less effectiveness against lung cancer with 80% cell viability. The results indicated that these DOX-loaded Kaolin and Kaolin intercalation compounds caused considerably higher cell death for breast cancer and digestive system cancers, including gastric cancer, colon cancer, and esophageal cancer, in a dose-dependent manner. Typically, the cell viabilities of gastric cancer were 13%–35% after incubation with the DOX-loaded nanoclays (except for that with DOX-Kaolin$_{MeOH}$, which was 67.94%).

Apoptosis was also detected using the DAPI staining method in cells treated with Kaolin and the Kaolin intercalation compounds. Chromatin condensation, nuclear shrinkage, and apoptotic body formation can easily be observed under fluorescence microscopy using DAPI staining. The results showed that all the nanoclays were unable to induce cell death, even at a high concentration (Fig. 5(a)). The apoptotic nuclei were seen to gradually increase with an increase in Kaolin and Kaolin intercalation compound concentration. Typically, CLSM has been used to study the internalization of Kaolin and Kaolin intercalation compounds into HeLa cancer cells. Figure 5(b) shows the subcellular location of the fabricated nanoclays in HeLa cells after incubation with fluorescein isothiocyanate (FITC)-labeled Kaolin and Kaolin intercalation compounds for 4 h. Lamp1 (a lysosome marker protein) antibody and DAPI were employed for lysosome and

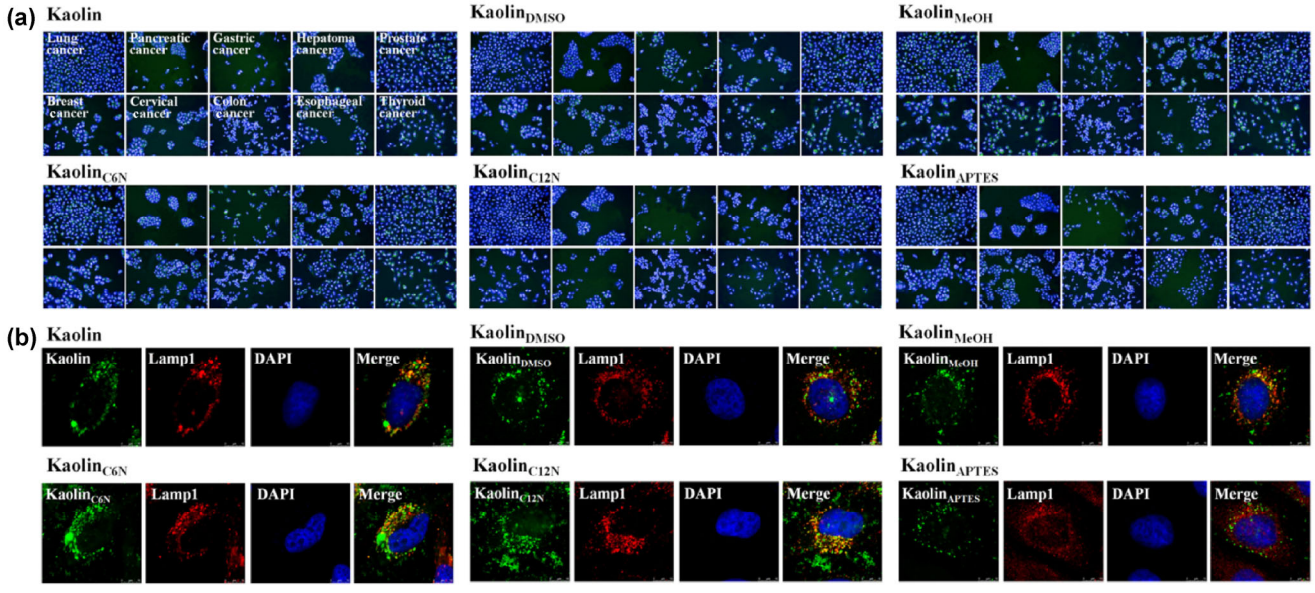

Figure 5 (a) DAPI and (b) CLSM images of cancer cells incubated with DOX-Kaolin and the DOX-Kaolin intercalation compounds at the concentration of 200 μg·mL^{-1}.

nuclei staining, respectively. The results showed that the FITC-Kaolin and FITC-Kaolin intercalation compounds (green) had good colocalization with lysosome (Lamp1, red), suggesting that most of the nanoclays had entered the lysosomes. The absence of fluorescent signals from the nuclei indicates that Kaolin and the Kaolin intercalation compounds could not pass through the nuclear membrane. The overlay of the bright field and fluorescent images further demonstrated that the luminescence correlated strongly with the intracellular location, suggesting the feasibility and efficiency of the nanocomposites for fluorescent cell imaging and anticancer drug delivery into cancerous cells. Based on the above analysis, it was concluded that the nanocomposites could be gradually taken up by the cells.

A mechanism was proposed to describe the action of the DOX-Kaolin and DOX-Kaolin intercalation compounds against cancer cells. At the cellular level, the DOX-loaded 2D nanoclays are intravenously implanted into the blood vessel and immediately internalized via endocytosis (Fig. S5 in the ESM) into endosomes, localized in the endolysosomes, and the DOX is then released and accumulated within the cell nucleus. Furthermore, more DOX is released from the DOX-loaded Kaolin and Kaolin intercalation compounds in the acidic microenvironment of the cancer cells than in macrophages because of the larger size and increased amount of acidic metabolic products in cancer cells than that in normal cells.

4 Conclusions

DDSs based on 2D Kaolin and Kaolin intercalation compounds were successfully prepared through the intercalation of organic guest species of various different chain lengths. Kaolin and the Kaolin intercalation compounds exhibited a high level of biocompatibility and very low toxicity towards most cancer cells. These fabricated nanoclays showed pH-responsive release behavior as well as enhanced therapeutic effect against ten model cancer cell cultures. Based on the results, Kaolin and the Kaolin intercalation compounds are concluded to be promising candidates for emerging DDSs and tissue engineering applications.

Acknowledgements

This work was supported by the National Natural Science Foundation of China (Nos. 51225403 and 41572036), the Hunan Provincial Science and Technology Project (Nos. 2016RS2004 and 2015TP1006), the Postdoctoral Science Foundation of Central South University (No. 155219) and the China Postdoctoral Science Foundation (No. 2015M582346).

Electronic Supplementary Material: Supplementary material (XRD, FTIR, TG, DSC, Bio-TEM results, N_2 adsorption–desorption isotherms, release profiles of DOX, viabilities of ten model cell cultures after incubated) is available in the online version of this article at https://doi.org/10.1007/s12274-017-1466-x.

References

[1] Dawson, J. I.; Oreffo, R. O. C. Clay: New opportunities for tissue regeneration and biomaterial design. *Adv. Mater.* **2013**, *25*, 4069–4086.

[2] Sun, T. M.; Zhang, Y. S.; Pang, B.; Hyun, D. C.; Yang, M. X.; Xia, Y. N. Engineered nanoparticles for drug delivery in cancer therapy. *Angew. Chem., Int. Ed.* **2014**, *53*, 12320–12364.

[3] Kemp, J. A.; Shim, M. S.; Heo, C. Y.; Kwon, Y. J. "Combo" nanomedicine: Co-delivery of multi-modal therapeutics for efficient, targeted, and safe cancer therapy. *Adv. Drug Deliv. Rev.* **2016**, *98*, 3–18.

[4] Damitz, R.; Chauhan, A. Parenteral emulsions and liposomes to treat drug overdose. *Adv. Drug Deliv. Rev.* **2015**, *90*, 12–23.

[5] Torchilin, V. P. Multifunctional, stimuli-sensitive nanoparticulate systems for drug delivery. *Nat. Rev. Drug Discov.* **2014**, *13*, 813–827.

[6] Howarth, A. J.; Liu, Y. Y.; Li, P.; Li, Z. Y.; Wang, T. C.; Hupp, J. T.; Farha, O. K. Chemical, thermal and mechanical stabilities of metal-organic frameworks. *Nat. Rev. Mater.* **2016**, *1*, 15018.

[7] Horcajada, P.; Gref, R.; Baati, T.; Allan, P. K.; Maurin, G.; Couvreur, P.; Férey, G.; Morris, R. E.; Serre, C. Metal-organic frameworks in biomedicine. *Chem. Rev.* **2012**, *112*, 1232–1268.

[8] Kean, T.; Thanou, M. Biodegradation, biodistribution and toxicity of chitosan. *Adv. Drug Deliv. Rev.* **2010**, *62*, 3–11.

[9] Park, J. H.; Saravanakumar, G.; Kim, K.; Kwon, I. C. Targeted delivery of low molecular drugs using chitosan

and its derivatives. *Adv. Drug Deliv. Rev.* **2010**, *62*, 28–41.

[10] Sun, C.; Lee, J. S. H.; Zhang, M. Q. Magnetic nanoparticles in MR imaging and drug delivery. *Adv. Drug Deliv. Rev.* **2008**, *60*, 1252–1265.

[11] Reddy, L. H.; Arias, J. L.; Nicolas, J.; Couvreur, P. Magnetic nanoparticles: Design and characterization, toxicity and biocompatibility, pharmaceutical and biomedical applications. *Chem. Rev.* **2012**, *112*, 5818–5878.

[12] Xu, C. J.; Sun, S. H. New forms of superparamagnetic nanoparticles for biomedical applications. *Adv. Drug Deliv. Rev.* **2013**, *65*, 732–743.

[13] Assa, F.; Jafarizadeh-Malmiri, H.; Ajamein, H.; Anarjan, N.; Vaghari, H.; Sayyar, Z.; Berenjian, A. A biotechnological perspective on the application of iron oxide nanoparticles. *Nano Res.* **2016**, *9*, 2203–2225.

[14] Hong, G. S.; Diao, S.; Antaris, A. L.; Dai, H. J. Carbon nanomaterials for biological imaging and nanomedicinal therapy. *Chem. Rev.* **2015**, *115*, 10816–10905.

[15] Bussy, C.; Methven, L.; Kostarelos, K. Hemotoxicity of carbon nanotubes. *Adv. Drug Deliv. Rev.* **2013**, *65*, 2127–2134.

[16] Chen, Y.; Tan, C. L.; Zhang, H.; Wang, L. Z. Two-dimensional graphene analogues for biomedical applications. *Chem. Soc. Rev.* **2015**, *44*, 2681–2701.

[17] Chen, Y.; Chen, H. R.; Shi, J. L. *In vivo* bio-safety evaluations and diagnostic/therapeutic applications of chemically designed mesoporous silica nanoparticles. *Adv. Mater.* **2013**, *25*, 3144–3176.

[18] Slowing, I. I.; Trewyn, B. G.; Giri, S.; Lin, V. S. Y. Mesoporous silica nanoparticles for drug delivery and biosensing applications. *Adv. Funct. Mater.* **2007**, *17*, 1225–1236.

[19] Slowing, I. I.; Vivero-Escoto, J. L.; Wu, C. W.; Lin, V. S. Y. Mesoporous silica nanoparticles as controlled release drug delivery and gene transfection carriers. *Adv. Drug Deliv. Rev.* **2008**, *60*, 1278–1288.

[20] Yu, M. H.; Niu, Y. T.; Zhang, J.; Zhang, H. W.; Yang, Y. N.; Taran, E.; Jambhrunkar, S.; Gu, W. Y.; Thorn, P.; Yu, C. Z. Size-dependent gene delivery of amine-modified silica nanoparticles. *Nano Res.* **2016**, *9*, 291–305.

[21] Luo, G. F.; Chen, W. H.; Jia, H. Z.; Sun, Y. X.; Cheng, H.; Zhuo, R. X.; Zhang, X. Z. An indicator-guided photo-controlled drug delivery system based on mesoporous silica/gold nanocomposites. *Nano Res.* **2015**, *8*, 1893–1905.

[22] Ariga, K.; Lvov, Y. M.; Kawakami, K.; Ji, Q. M.; Hill, J. P. Layer-by-layer self-assembled shells for drug delivery. *Adv. Drug Deliv. Rev.* **2011**, *63*, 762–771.

[23] Wang, Q.; O'Hare, D. Recent advances in the synthesis and application of layered double hydroxide (LDH) nanosheets. *Chem. Rev.* **2012**, *112*, 4124–4155.

[24] Choi, S. J.; Choy, J. H. Layered double hydroxide nanoparticles as target-specific delivery carriers: Uptake mechanism and toxicity. *Nanomedicine* **2011**, *6*, 803–814.

[25] Lvov, Y.; Wang, W. C.; Zhang, L. Q.; Fakhrullin, R. Halloysite clay nanotubes for loading and sustained release of functional compounds. *Adv. Mater.* **2016**, *28*, 1227–1250.

[26] Vergaro, V.; Abdullayev, E.; Lvov, Y. M.; Zeitoun, A.; Cingolani, R.; Rinaldi, R.; Leporatti, S. Cytocompatibility and uptake of halloysite clay nanotubes. *Biomacromolecules* **2010**, *11*, 820–826.

[27] Lvov, Y.; Aerov, A.; Fakhrullin, R. Clay nanotube encapsulation for functional biocomposites. *Adv. Colloid Interface Sci.* **2014**, *207*, 189–198.

[28] Tully, J.; Yendluri, R.; Lvov, Y. Halloysite clay nanotubes for enzyme immobilization. *Biomacromolecules* **2016**, *17*, 615–621.

[29] Niu, M. Y.; Yang, H. M.; Zhang, X. C.; Wang, Y. T.; Tang, A. D. Amine-impregnated mesoporous silica nanotube as an emerging nanocomposite for CO_2 capture. *ACS Appl. Mater. Interfaces* **2016**, *8*, 17312–17320.

[30] Li, X. Y.; Yang, Q.; Ouyang, J.; Yang, H. M.; Chang, S. Chitosan modified halloysite nanotubes as emerging porous microspheres for drug carrier. *Appl. Clay Sci.* **2016**, *126*, 306–312.

[31] Niu, M. Y.; Li, X. Y.; Ouyang, J.; Yang, H. M. Lithium orthosilicate with halloysite as silicon source for high temperature CO_2 capture. *RSC Adv.* **2016**, *6*, 44106–44112.

[32] Jin, J.; Fu, L. J.; Yang, H. M.; Ouyang, J. Carbon hybridized halloysite nanotubes for high-performance hydrogen storage capacities. *Sci. Rep.* 2015, *5*, 12429.

[33] Corrales, T.; Larraza, I.; Catalina, F.; Portolés, T.; Ramírez-Santillán, C.; Matesanz, M.; Abrusci, C. *In vitro* biocompatibility and antimicrobial activity of poly(ε-caprolactone)/montmorillonite nanocomposites. *Biomacromolecules* **2012**, *13*, 4247–4256.

[34] Wang, Z. Y.; Zhu, W. P.; Qiu, Y.; Yi, X.; von dem Bussche, A.; Kane, A.; Gao, H. J.; Koski, K.; Hurt, R. Biological and environmental interactions of emerging two-dimensional nanomaterials. *Chem. Soc. Rev.* **2016**, *45*, 1750–1780.

[35] Durak, G. M.; Taylor, A. R.; Walker, C. E.; Probert, I.; de Vargas, C.; Audic, S.; Schroeder, D.; Brownlee, C.; Wheeler, G. L. A role for diatom-like silicon transporters in calcifying coccolithophores. *Nat. Commun.* **2016**, *7*, 10543.

[36] Delalat, B.; Sheppard, V. C.; Ghaemi, S. R.; Rao, S. S.; Prestidge, C. A.; McPhee, G.; Rogers, M.-L.; Donoghue, J. F.; Pillay, V.; Johns, T. G. et al. Targeted drug delivery using genetically engineered diatom biosilica. *Nat. Commun.* **2015**, *6*, 8791.

[37] Maher, S.; Alsawat, M.; Kumeria, T.; Fathalla, D.; Fetih, G.; Santos, A.; Habib, F.; Losic, D. Luminescent silicon diatom replicas: Self-reporting and degradable drug carriers with biologically derived shape for sustained delivery of therapeutics. *Adv. Funct. Mater.* **2015**, *25*, 5107–5116.

[38] Liu, S. Y.; Yang, H. M. Composite of coal-series kaolinite and capric-lauric acid as form-stable phase-change material. *Energy Technol*. **2015**, *3*, 77–83.

[39] Tan, D. Y.; Yuan, P.; Annabi-Bergaya, F.; Liu, D.; He, H. P. Methoxy-modified kaolinite as a novel carrier for high-capacity loading and controlled-release of the herbicide amitrole. *Sci. Rep.* **2015**, *5*, 8870.

[40] Ghadiri, M.; Chrzanowski, W.; Rohanizadeh, R. Biomedical applications of cationic clay minerals. *RSC Adv.* **2015**, *5*, 29467–29481.

[41] Ding, W. J.; Ouyang, J.; Yang, H. M. Synthesis and characterization of nesquehonite ($MgCO_3{\cdot}3H_2O$) powders from natural talc. *Powder Technol.* **2016**, *292*, 169–175.

[42] He, X.; Yang, H. M. Fluorescence and room temperature activity of Y_2O_3:(Eu^{3+},Au^{3+})/palygorskite nanocomposite. *Dalton Trans.* **2015**, *44*, 1673–1679.

[43] Hu, P. W.; Yang, H. M. Insight into the physicochemical aspects of kaolins with different morphologies. *Appl. Clay Sci.* **2013**, *74*, 58–65.